Novelty Journals

ISSN 2394-7349

International Journal of Novel Research in Engineering and Science
Vol. 13, Issue 1, pp: (24-37), Month: March 2026 - August 2026, Available at: www.noveltyjournals.com

Heat Exchange Phenomena of Ag–GO Hybrid Nanofluid in a Rotating Porous Medium under MHD, Thermal Radiation, and Joule Heating

C Sulochana[1*], Nityanand[1]

[1]Department of mathematics, Gulbarga University, Kalaburagi, Karnataka.

DOI: https://doi.org/10.5281/zenodo.20508593

Published Date: 02-June-2026

Abstract: **This research investigates the magnetohydrodynamic (MHD) flow and thermal transport characteristics of a silver–graphene oxide (Ag–GO) composite nanofluid within a rotating arrangement formed by a pair of parallel plates. The working fluid consists of a 50:50 water–ethylene glycol combination. The mathematical formulation includes heat radiation, Joule heating, and Darcy resistance to represent porous medium influences, while both the upper and lower plates are assumed to be permeable and stretchable, respectively. Appropriate similarity transformations transform the governing coupled nonlinear ordinary differential equations into dimensionless form, and the resulting equations are solved numerically using the MATLAB bvp4c technique. The effects of several important parameters, including Darcy number, magnetic parameter, rotation parameter, suction/blowing parameter, radiation parameter, Reynolds number, and nanoparticle volume fraction, are examined in detail. The findings reveal that higher Darcy resistance reduces fluid velocity while increasing temperature distribution. Furthermore, the incorporation of Ag–GO nanoparticles considerably enhances thermal performance. The Nusselt number rises with greater nanoparticle concentration and fluid injection, whereas it declines as porous resistance increases.**

Keywords: **Hybrid Nanofluid (HNF), Heat Transfer, Rotating System, Magnetohydrodynamics (MHD), Thermal Conductivity, Joule Heating.**

I. INTRODUCTION

Nanofluids, which contain nanoparticles suspended within a carrier liquid, have gained significant interest because of their improved thermal efficiency in comparison with traditional fluids. Their higher thermal conductivity, better heat transfer capability, and durable stability characteristics make them highly appropriate for numerous industrial and technological applications [1]. In recent times, hybrid nanofluids, produced through the incorporation of two or more different nanoparticles, have developed into an important category of advanced heat transfer fluids.

Consequently, both convective and conductive modes of heat transfer are greatly affected by elements including nanoparticle concentration fraction, rotational velocity, and fluid characteristics [5]. Understanding these influences is important for applications involving rotating equipment, including gas turbines, rotary heat exchangers, and cooling technologies used in microelectronic systems. The incorporation of hybrid nanofluids into rotating configurations offers an effective approach for improving thermal performance because of their excellent heat transport properties [6,7]. The combined influence of rotational motion and nanoparticle-based enhancement produces complex flow characteristics, requiring detailed analysis. Heat transfer in rotating configurations, especially over rotating disks and parallel plates, has attracted growing interest because of its extensive applications in aerospace technology, power systems, chemical industries, and biomedical engineering [8–10]. Earlier investigations have shown that the thermophysical characteristics of composite nanofluids, such as thermal conductive capability, dynamic viscosity, and specific thermal capacity, serve a major function in evaluating their effectiveness in such applications [11,12]. A substantial amount of research has been carried out on hybrid nanofluid flow under different physical situations. For example, Preetham et al. [13] examined magnetohydrodynamic (MHD) hybrid nanofluid flow in a rotating configuration using a Fibonacci wavelet collocation

technique. Similarly, Shah et al. [14] explored the thermal characteristics of TiO_2–Fe_3O_4 hybrid nanofluid and reported improved heat transfer behavior. Arshad et al. [16] analyzed rotational hybrid nanofluid flow with chemical reaction and thermal radiation through MATLAB-oriented numerical approaches. Moatimid et al. [17] examined nonlinear viscous Casson type fluid flow behaviour in a rotating conical arrangement, while Tian et al. [18] evaluated the performance of hybrid nanofluids in thermal sink applications. Additional contributions by Roy et al. [19] and Fazeli et al. [20] also emphasized the significance of composite nanofluids in enhancing thermal transport phenomena.

Furthermore, the effects of porous materials, thermal radiation, and Joule heating on hybrid nanofluid motion have been extensively examined. Yasmin et al. [24] employed the Brinkman formulation to investigate MHD nanofluid flow inside a porous cavity, whereas Siddiqa et al. [25] analyzed conjugate heat transfer phenomena in micropolar nanofluids. Yacob et al. [26] studied rotating nanofluid flow using the bvp4c numerical technique. More recent investigations have concentrated on multiphysical interaction effects. Shoaib et al. [27–29] explored MHD radiative hybrid nanofluid flow and observed notable enhancement in heat transfer performance. Abu Bakar et al. [30] highlighted the significance of permeability in porous structures, while Rashad [31] and Jecelani et al. [32] examined the influence of radiation and porous effects on thermal behavior. Khalil et al. [33] demonstrated the contribution of Joule heating and electrical conductivity to entropy generation, and Alharbi et al. [35] emphasized the importance of Darcy–Forchheimer effects in graphene-based hybrid nanofluids. Recent investigations [36] also verified that rotational and viscous dissipation effects strongly affect temperature distribution in hybrid nanofluid systems.

Despite these developments, only limited research has addressed the combined impact of porous resistance, rotational motion, magnetic effects, thermal radiation, and Joule heating on Ag–GO hybrid nanofluids within a parallel-plate arrangement. In particular, the contribution of the Darcy parameter in controlling both primary and secondary velocity distributions, along with its effect on thermal transport behavior in rotating hybrid nanofluid systems, still requires further investigation.

Driven by this research gap, the present work analyzes the magnetohydrodynamic flow and thermal transport behavior of an Ag–GO hybrid nanofluid using a water–ethylene glycol (50:50) mixture in a rotating porous medium between parallel plates. The mathematical model incorporates the simultaneous influences of thermal radiation, Joule heating, and Darcy resistance. The governing nonlinear partial differential equations are transformed into a set of coupled ordinary differential equations through suitable similarity transformations and solved numerically using the MATLAB bvp4c approach. The influence of significant physical parameters, including Darcy parameter, magnetic parameter, rotation parameter, Reynolds number, suction/blowing parameter, and radiation parameter, is investigated comprehensively. Particular attention is devoted to understanding the interaction between porous resistance and improved thermal conductivity of the hybrid nanofluid, together with their combined effects on velocity profiles and heat transfer performance.

In contrast to previous investigations, the current study presents a coupled examination of Darcy-regulated porous resistance with Ag–GO hybrid nanofluid flow in a rotating parallel-plate configuration, where the simultaneous effects of Coriolis forces, Lorentz forces, and permeability are quantified in terms of thermal enhancement. Additionally, the effect of Darcy number on secondary flow characteristics and Nusselt number behavior in a rotating hybrid nanofluid configuration has not been reported previously.

II. PROBLEM DESCRIPTION

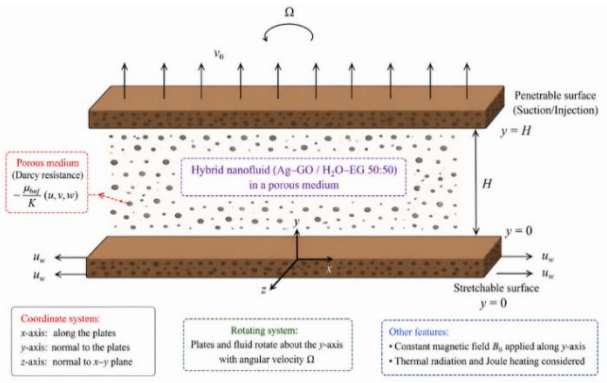

Fig.1 Geometry of the problem

Assume an incompressible viscous hybrid nanofluid experiencing steady laminar radiative motion between two parallel plates, where one surface is stretchable while the opposite surface is permeable (Fig. 1). The flow region is filled with a uniform porous material, and the resistance generated by the porous structure is represented through the Darcy model. The plates are positioned at (y = 0) and (y = h). The complete system rotates about the z-axis with a constant angular velocity (Ω). The x-axis is aligned along the plate surface, the y-axis is taken perpendicular to the plates, and the z-axis is normal to the x–y plane. The porous medium produces a resistive drag force directly related to the velocity components, which is governed by the permeability of the medium through the Darcy parameter. Furthermore, a uniform magnetic field of intensity (B_0) is imposed normal to the plates along the y-axis. The thermophysical characteristics of the Ag–GO hybrid nanofluid, with a water–ethylene glycol (50:50) mixture as the carrier fluid, are listed in Table I. Based on these assumptions, the governing equations for conservation of mass, momentum, and energy representing the steady motion of the hybrid nanofluid in a rotating porous environment are established.

$$\frac{\partial u}{\partial x}+\frac{\partial v}{\partial y}=0 \tag{1}$$

$$u\left(\frac{\partial u}{\partial x}\right)+v\left(\frac{\partial u}{\partial y}\right)+2\Omega w=-\frac{1}{\rho_{hnf}}\left(\frac{\partial p}{\partial x}\right)+\nu_{hnf}\left(\frac{\partial^2 u}{\partial x^2}+\frac{\partial^2 u}{\partial y^2}\right)-\frac{\sigma_{hnf}B_0^2}{\rho_{hnf}}u-\frac{\nu_{hnf}}{K_1}u \tag{2}$$

$$u\left(\frac{\partial v}{\partial x}\right)+v\left(\frac{\partial v}{\partial y}\right)=-\frac{1}{\rho_{hnf}}\left(\frac{\partial p}{\partial y}\right)+\nu_{hnf}\left(\frac{\partial^2 v}{\partial x^2}+\frac{\partial^2 v}{\partial y^2}\right)-\frac{\nu_{hnf}}{K_1}v \tag{3}$$

$$u\left(\frac{\partial w}{\partial x}\right)+v\left(\frac{\partial w}{\partial y}\right)-2\Omega u=\nu_{hnf}\left(\frac{\partial^2 w}{\partial x^2}+\frac{\partial^2 w}{\partial y^2}\right)-\frac{\sigma_{hnf}B_0^2}{\rho_{hnf}}w-\frac{\nu_{hnf}}{K_1}w \tag{4}$$

$$v\frac{\partial T}{\partial y}+u\frac{\partial T}{\partial x}+w\frac{\partial T}{\partial z}=\frac{k_{hnf}}{(\rho C_p)_{hnf}}\left(\frac{\partial^2 T}{\partial x^2}+\frac{\partial^2 T}{\partial y^2}+\frac{\partial^2 T}{\partial z^2}\right)-\frac{1}{(\rho C_p)_{hnf}}\frac{\partial q_{rad}}{\partial y}+\frac{\sigma_f B_0^2}{(\rho C_p)_{hnf}}(u^2+w^2) \tag{5}$$

In the current mathematical model, the quantities $\Omega, w, v, u, B_0, P, \sigma_f, T, q_{rad}$ and k represent the rotational speed, axial flow component (along the z-axis), velocity component along the y-direction, velocity component along the x-direction, externally applied magnetic field intensity, fluid pressure, electrical conductivity, temperature distribution, radiative heat transfer flux, and permeability coefficient of the porous structure, respectively. Equation (4) further indicates that no pressure variation exists in the axial direction, which confirms the absence of cross-flow motion along the z-axis. To account for thermal radiation phenomena, the Rosseland diffusion approximation is adopted.

$$q_{rad}=-\left(\frac{4\sigma^*}{3k^*_{hnf}}\right)\frac{\partial T^4}{\partial y} \tag{6}$$

Within the present analysis, σ^* denotes the Stefan–Boltzmann constant, whereas k^*_{hnf} refers to the average absorption parameter associated with the hybrid nanofluid. In addition, the temperature difference inside the flow region is considered to be relatively small, which permits the nonlinear term $T^4$to be approximated through a Taylor series expansion around the surrounding temperature T_∞.

$$T^4\approx -3T_\infty^4+4T_\infty^3T \tag{7}$$

By neglecting higher-order terms, a simplified expression is obtained for further analysis.

$$u\frac{\partial T}{\partial x}+v\frac{\partial T}{\partial y}+w\frac{\partial T}{\partial z}=\frac{k_{hnf}}{(\rho C_p)_{hnf}}\left(\frac{\partial^2 T}{\partial x^2}+\frac{\partial^2 T}{\partial y^2}+\frac{\partial^2 T}{\partial z^2}\right)+\frac{16\sigma^*T_\infty^3}{3k^*_{nf}(\rho C_p)_{hnf}}\frac{\partial^2 T}{\partial y^2}+\frac{\sigma_f B_0^2}{(\rho C_p)_{hnf}}(u^2+w^2) \tag{8}$$

where ρ_{hnf} denotes the effective density, μ_{hnf} represents the effective dynamic viscosity, $(\rho Cp)_{hnf}$ indicates the effective heat capacitance, and k_{hnf} corresponds to the effective thermal conductivity of the hybrid nanofluid.

$$\rho_{hnf} = (1-\phi_{Cu}-\phi_{Go})\rho_f + \phi_{Cu}\rho_{Cu} + \phi_{Go}\rho_{Go}$$

$$(\rho C_p)_{hnf} = (1-\phi_{Cu}-\phi_{Go})(\rho C_p)_f + \phi_{Cu}(\rho C_p)_{Cu} + \phi_{Go}(\rho C_p)_{Go}$$

$$\mu_{hnf} = \mu_f(1-\phi_{Cu}-\phi_{Go})^{-2.5} \tag{9}$$

$$\frac{k_{hnf}}{k_f} = \left\{\frac{k_{Cu}\phi_{Cu}+k_{Go}\phi_{Go}}{\phi_{Cu}+\phi_{Go}} + 2k_f + 2(k_{Cu}\phi_{Cu}+k_{Go}\phi_{Go}) - 2(\phi_{Cu}+\phi_{Go})k_f\right\} \times \left\{\frac{k_{Cu}\phi_{Cu}+k_{Go}\phi_{Go}}{\phi_{Cu}+\phi_{Go}} + 2k_f - (k_{Cu}\phi_{Cu}+k_{Go}\phi_{Go}) + (\phi_{Cu}+\phi_{Go})k_f\right\}^{-1}$$

The associated boundary conditions are expressed as

$u = u_w = ax,\ w = 0,\ v = 0,\ T = T_H$ at $y = 0$

$u = 0,\ w = 0,\ v = v_0,\ T = T_0$ at $y = h$ (10)

We define the following similarity variables:

$$\eta = \frac{y}{h},\ v = -ahf(\eta),\ u = axf'(\eta),\ w = axg(\eta),\ \theta = \frac{T-T_H}{T_0-T_H} \tag{11}$$

TABLE I. Thermophysical characteristics of water–Ethylene Glycol (50:50) and nanoparticles

	$\rho(kg/m^3)$	$Cp(J/kg\ K)$	$k(W/m\ K)$
Silver (Ag)	10500	235	429
Graphene Oxide (Go)	1800	717	5000
water-Ethyle Glycol (50-50)	1056	3288	0.425

By substituting these physical relations into the governing equations and eliminating the pressure gradient terms, the resulting coupled nonlinear ordinary differential equations governing momentum and thermal transport are obtained as follows:

$$f^{iv} + B_1(1-\phi_{Cu}-\phi_{Go})^{2.5}Re(ff''' - f'f'') - 2B_1Ro(1-\phi_{Cu}-\phi_{Go})^{2.5}g' - \mathrm{Mn}(1-\phi_{Cu}-\phi_{Go})^{2.5}f'' - \frac{1}{Da}f' = 0 \tag{12}$$

$$g'' + B_1(1-\phi_{Cu}-\phi_{Go})^{2.5}Re\,(fg' - f'g) + 2B_1Ro(1-\phi_{Cu}-\phi_{Go})^{2.5}f' - \mathrm{Mn}(1-\phi_{Cu}-\phi_{Go})^{2.5}g - \frac{1}{Da}g = 0 \tag{13}$$

$$\theta'' + B_2\,\mathrm{Pr}\,\mathrm{Re}\left(\frac{3}{3+4N}\right)\frac{k_f}{k_{hnf}}f\theta' + \mathrm{Mn}\,\mathrm{Pr}\,\mathrm{Ec}\left(\frac{3}{3+4N}\right)\frac{k_f}{k_{hnf}}(f'^2+g'^2) = 0 \tag{14}$$

The Darcy number is expressed as Da = K / L², where K denotes the permeability coefficient of the porous structure.

The constants A1, A2, B1 and B2 are defined as follows.

$$A_1 = (1-\phi_{Cu}-\phi_{Go})^{-2.5}$$

$$A_2 = \frac{k_{hnf}}{k_f}$$

$$B_1 = (1-\phi_{Cu}-\phi_{Go}) + \frac{\phi_{Cu}\rho_{Cu}+\phi_{Go}\rho_{Go}}{\rho_f}$$

$$B_2 = (1-\phi_{Cu}-\phi_{Go}) + \frac{\phi_{Cu}(\rho C_p)_{Cu}+\phi_{Go}(\rho C_p)_{Go}}{(\rho C_p)_f} \tag{15}$$

Subject to the following boundary conditions:

$$f(0) = 0,\ f(1) = A,\ f'(0) = 1,\ f'(1) = 0,$$

$$g(1) = 0,\ g(0) = 0,\ \theta(0) = 1,\ \theta(1) = 0 \quad (16)$$

where $Pr, Ro, Re, Mn, N, Ec,\ A$ and Da denote the Prandtl number, rotation parameter, Reynolds number, magnetic parameter, radiation parameter, Eckert number, suction or injection parameter and Darcy parameter respectively. It should be noted that $A > 0$ corresponds to injection flow, whereas $A < 0$ indicates suction flow.

III. PARAMETERS OF ENGINEERING INTEREST

A. Skin friction coefficient and Nusselt number

Additional important engineering quantities considered in the current investigation include the skin friction coefficient and the Nusselt number, which are expressed as follows:

$$C_f^* = \frac{\mu_{hnf}}{\rho_f v_0^2}\frac{\partial u}{\partial y}\bigg|_{y=0}$$

$$Nu^* = -\left[\frac{h}{k_f(T_0 - T_H)}\right]\left(k_{hnf} + \frac{16\sigma^* T_\infty^3}{3k_{hnf}^*}\right)\frac{\partial T}{\partial y}\bigg|_{y=0} \quad (17)$$

Using Eqs. (9) and (11), we obtain:

$$C_f = |(1 - \phi_{Cu} - \phi_{Go})^{-2.5} f''(0)|$$

$$Nu = \left|\frac{k_{hnf}}{k_f}\left(1 + \frac{4}{3}N\right)\theta'(0)\right| \quad (18)$$

IV. NUMERICAL PROCEDURE

The transformed nonlinear ordinary differential equation system together with the corresponding boundary conditions is solved numerically through the finite-difference collocation technique available in the MATLAB built-in solver bvp4c. For efficient numerical implementation, the higher-order differential equations are initially converted into an equivalent set of first-order ordinary differential equations by applying the following variable transformations:

$$y_1 = f,\ y_2 = f',\ y_3 = f'',\ y_4 = f''',\ y_5 = g,\ y_6 = g',\ y_7 = \theta,\ y_8 = \theta'$$

Using these transformations, the governing equations are rewritten as:

$$\frac{dy_1}{d\eta} = y_2,$$

$$\frac{dy_2}{d\eta} = y_3,$$

$$\frac{dy_3}{d\eta} = y_4,$$

$$\frac{dy_4}{d\eta} = B_1 A_1 Re(y_2 y_3 - y_1 y_4) + 2B_1 Ro A_1 y_6 + Mn A_1 y_3 - \frac{1}{Da} y_2,$$

$$\frac{dy_5}{d\eta} = y_6,$$

$$\frac{dy_6}{d\eta} = B_1 A_1 Re(y_2 y_5 - y_1 y_6) - 2B_1 Ro A_1 y_2 + Mn A_1 y_5 - \frac{1}{Da} y_5,$$

Novelty Journals

ISSN 2394-7349

International Journal of Novel Research in Engineering and Science
Vol. 13, Issue 1, pp: (24-37), Month: March 2026 - August 2026, Available at: www.noveltyjournals.com

$$\frac{dy_7}{d\eta} = y_8,$$

$$\frac{dy_8}{d\eta} = \frac{-B_2 PrRe\, y_1 y_8 \left(\frac{3}{3+4N}\right) - MnPrEc \left(\frac{3}{3+4N}\right)(y_2^2 + y_5^2)}{A_2}$$

The corresponding boundary conditions become:

$$y_1(0) = 0,\ y_2(0) = 1,\ y_5(0) = 0,\ y_7(0) = 1,$$
$$y_1(1) = A,\ y_2(1) = 0,\ y_5(1) = 0,\ y_7(1) = 0$$

An initial guess satisfying the boundary conditions is provided to start the iteration process. The computational domain 0≤ η ≤10 is discretized using a uniform mesh, and the solver iteratively refines the solution until the desired convergence tolerance is achieved.

The accuracy and convergence of the numerical solution are ensured by verifying the stability of results with mesh refinement and comparing with limiting cases available in the literature.

V. RESULT AND DISCUSSION

The transformed set of nonlinear ordinary differential equations (Eqs. (12)–(14)), together with the associated boundary conditions, is solved numerically using the MATLAB inbuilt collocation solver bvp4c. The numerical implementation is performed by reducing the higher-order differential equations into an equivalent collection of first-order differential equations through appropriate variable substitutions. A sufficiently refined computational mesh along with suitable initial approximations is utilized to guarantee the convergence and reliability of the obtained numerical results.

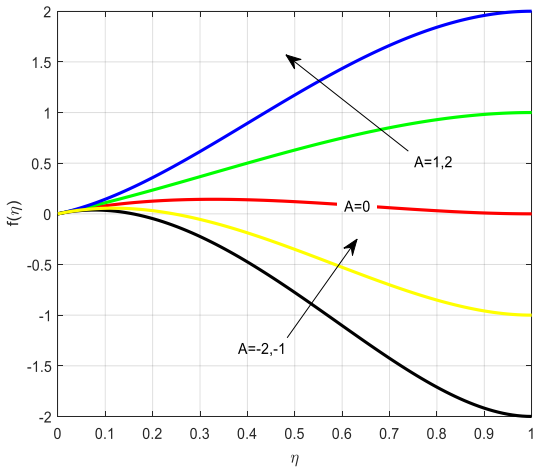

2a

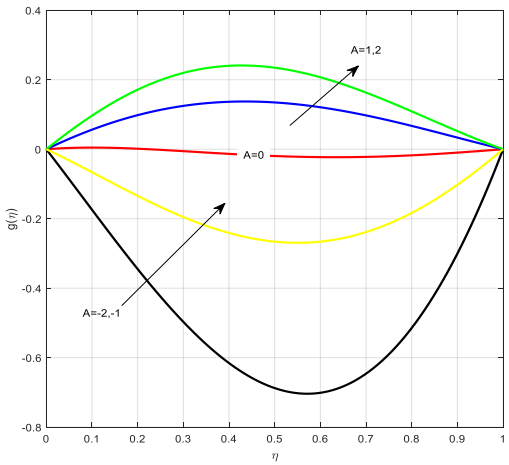

2b

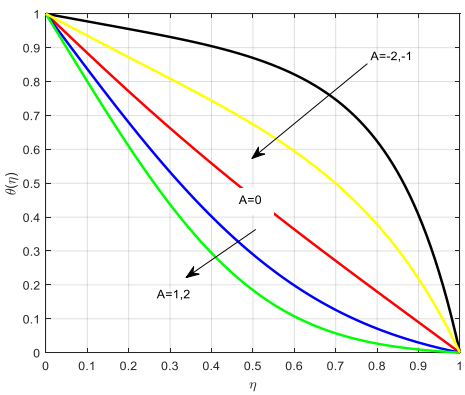

2c

Fig. 2 Influence of Suction/Injection Parameter (A) on Velocity Distribution and Temperature Characteristics.

Figure 2a presents the behavior of axial velocity $f'(\eta)$ for various values of the suction/injection parameter A . It can be observed that for positive values of A (suction), the velocity distribution increases noticeably. In contrast, negative values of A (injection) reduce the velocity magnitude and may even produce negative velocity within the flow region. Physically, suction strengthens boundary layer stability by extracting fluid from the surface, thereby decreasing momentum boundary layer thickness and improving fluid movement along the plate. On the other hand, injection introduces additional fluid into the system, which enlarges the boundary layer and weakens axial motion. This behavior causes a decline in velocity magnitude and may lead to flow reversal under strong injection conditions. Figure 2b demonstrates the influence of A on the secondary velocity component $g(\eta)$. It is evident that increasing positive values of A (suction) considerably enhance the secondary velocity profile. Conversely, negative values of A (injection) generate an opposite trend, causing the velocity to become progressively negative. The secondary motion is strongly affected by rotational and cross-flow phenomena. Suction improves transverse momentum transport, thereby reinforcing the secondary flow structure, whereas injection disturbs the organized motion and lowers effective momentum transfer, resulting in weaker secondary flow behavior. From Figure 2c, it is observed that increasing A (suction) reduces the temperature profile throughout the flow domain. Meanwhile, injection (A < 0) produces higher temperature distributions. This phenomenon occurs because suction removes heated fluid from the boundary region, which decreases thermal boundary layer thickness and enhances heat transfer performance. In contrast, injection supplies warmer fluid into the flow field, increasing thermal boundary layer thickness and lowering the heat transfer rate, thereby leading to elevated temperature levels.

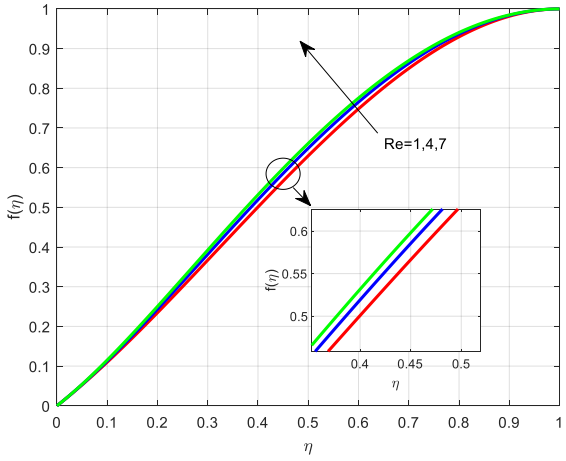

3a

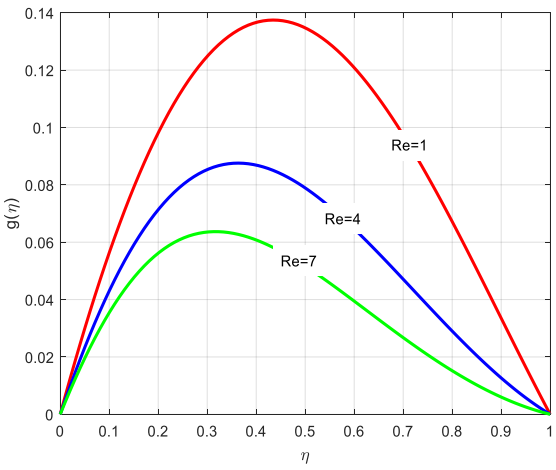

3b

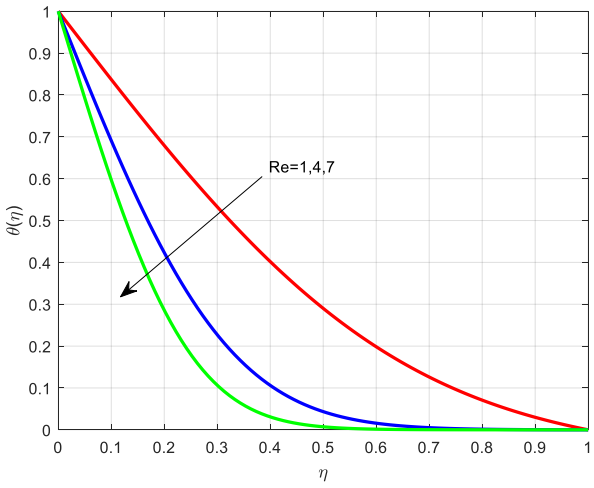

3c

Fig. 3 Influence of Reynolds Number Re on Velocity Distribution and Temperature Characteristics.

Figure 3a illustrates the effect of the Reynolds number on axial velocity. It is observed that an increase in Re produces a moderate rise in the velocity profile. From a physical viewpoint, a larger Reynolds number indicates stronger inertial influences compared with viscous forces. As a result, viscous resistance decreases, allowing the fluid to travel more easily and thereby increasing the velocity magnitude. Nevertheless, the enhancement remains moderate because of the additional resistive influences generated by magnetic and porous medium effects. Figure 3b presents the variation of secondary velocity with Re. It can be seen that increasing Reynolds number reduces the magnitude of the secondary velocity component. The reduction in secondary flow is mainly associated with the dominance of inertial forces, which suppress rotationally induced cross-flow motion. As inertia becomes stronger, the flow aligns more closely with the primary direction, thereby weakening the secondary velocity behavior. Figure 3c displays the temperature distribution for different values of Re . It is evident that higher Reynolds number considerably lowers the temperature profile. This behavior occurs because increasing Reynolds number strengthens convective transport, which promotes the removal of heat from the surface region. Consequently, the thermal boundary layer becomes thinner, resulting in reduced temperature levels throughout the flow domain.

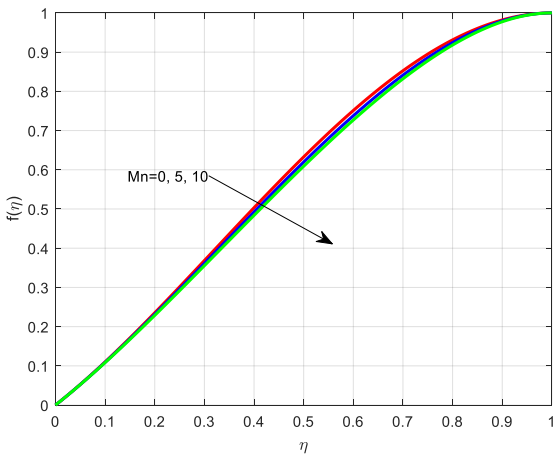

4a

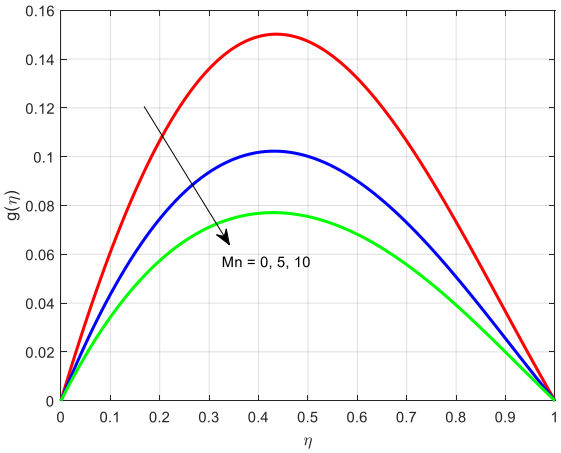

4b

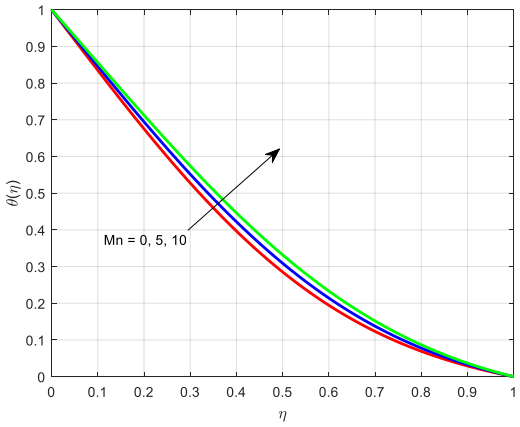

4c

Fig. 4 Influence of Magnetic Number Mn on Velocity Distribution and Temperature Characteristics.

Figure 4a demonstrates the effect of the magnetic parameter Mn on the axial velocity profile. It is noticed that increasing values of Mn lead to a slight decline in the axial velocity $f(\eta)$. This trend occurs because the applied magnetic field generates a Lorentz force that acts opposite to the motion of the electrically conducting hybrid nanofluid. Consequently, fluid momentum is reduced, producing a decrease in velocity. However, the reduction remains moderate because of the competing influences of inertial and rotational forces present in the system. Figure 4b presents the behavior of the secondary

velocity component $g(\eta)$ for different values of Mn. It is clearly observed that larger magnetic parameter values significantly decrease the magnitude of the secondary velocity. Physically, the magnetic field suppresses transverse fluid motion more strongly than axial motion because of the interaction between rotational and cross-flow effects. The Lorentz force weakens the rotationally generated secondary flow, thereby reducing the cross-flow structure. As a result, the secondary velocity decreases noticeably with increasing Mn. Figure 4c illustrates the temperature distribution for varying magnetic parameter values. It is evident that increasing Mn raises the temperature profile $\theta(\eta)$. The increase in temperature is mainly associated with the transformation of kinetic energy into thermal energy caused by magnetic damping, commonly referred to as the Joule heating effect. The suppression of fluid motion weakens convective heat transport while simultaneously producing additional heat within the fluid region. Therefore, the thermal boundary layer becomes thicker, leading to elevated temperature distributions.

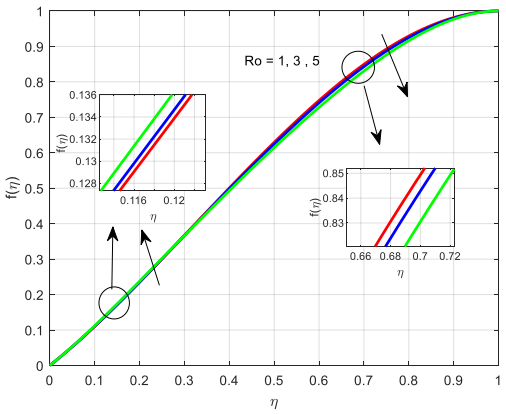

5a

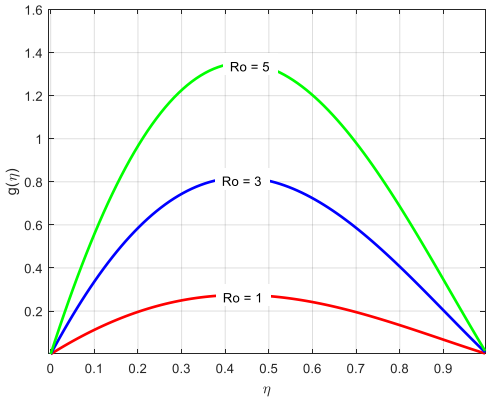

5b

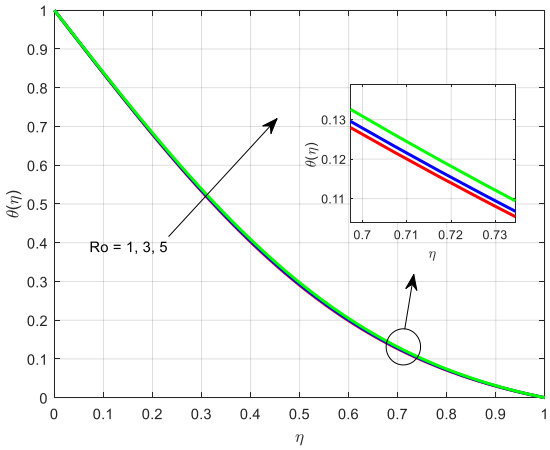

5c

Fig. 5 Influence of Rotation Parameter Ro on Velocity Distribution and Temperature Characteristics.

Figure 5a illustrates the influence of the rotation parameter Ro on axial velocity. It is observed that increasing Ro causes a slight decrease in the axial velocity profile. The rotational motion of the system generates Coriolis forces, which redistribute momentum between the axial and transverse directions. As rotational intensity increases, a portion of the axial momentum is transferred into secondary motion, producing a moderate reduction in the primary velocity component. Figure 5b depicts the effect of the rotation parameter Ro on the secondary velocity profile. It can be clearly seen that larger values of Ro significantly enhance the secondary velocity $g(\eta)$. This behavior occurs because stronger rotation intensifies Coriolis forces, which promote transverse fluid motion and strengthen the secondary flow structure. Consequently, the peak magnitude of $g(\eta)$ rises considerably with increasing rotational rate. Figure 5c presents the temperature distribution for

Novelty Journals

ISSN 2394-7349

International Journal of Novel Research in Engineering and Science
Vol. 13, Issue 1, pp: (24-37), Month: March 2026 - August 2026, Available at: www.noveltyjournals.com

different values of . It is evident that increasing Ro results in a slight rise in temperature. The enhancement in temperature is associated with rotational motion, which alters the flow configuration and weakens convective heat transfer efficiency. The redistribution of momentum reduces axial heat transport, leading to a mild increase in thermal boundary layer thickness and therefore producing higher temperature profiles throughout the flow region.

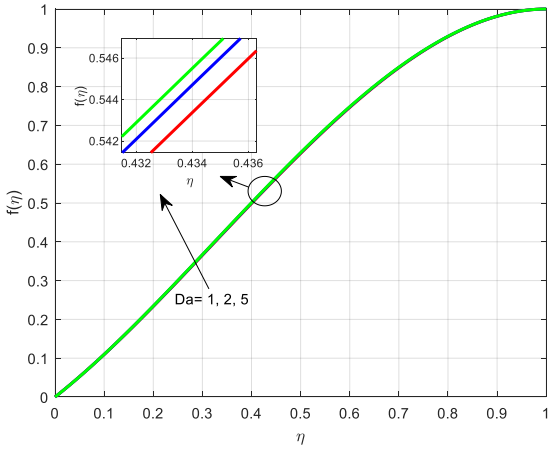

6a

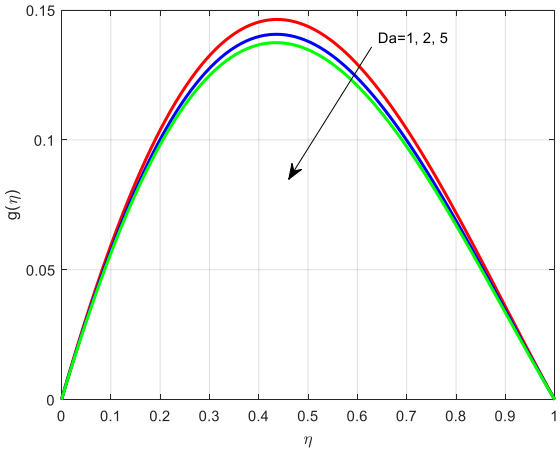

6b

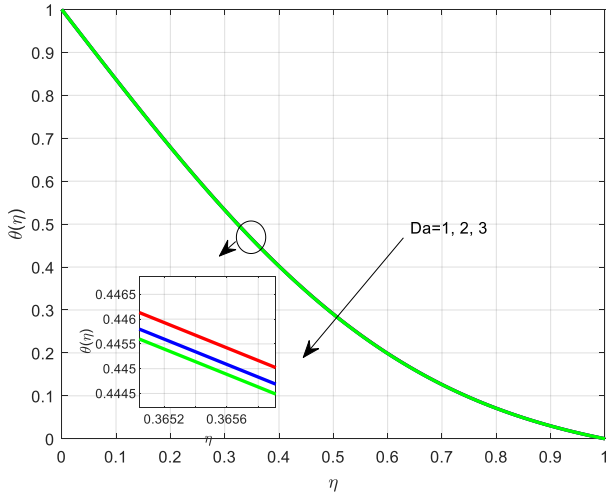

6c

Fig. 6 Influence of Darcy Parameter Da on Velocity Distribution and Temperature Characteristics.

Figure 6a demonstrates the effect of the Darcy parameter Da on the axial velocity profile. It is observed that increasing Da produces a slight improvement in the axial velocity $f(\eta)$. From a physical perspective, the Darcy parameter characterizes the permeability of the porous medium. Larger values of Da indicate greater permeability, which lowers the resistance imposed by the porous structure on fluid motion. Consequently, the drag force within the porous region decreases, enabling the fluid to move more easily and thereby increasing the velocity magnitude. However, the enhancement remains moderate because of the simultaneous action of magnetic and rotational resistive effects. Figure 6b presents the variation of secondary velocity $g(\eta)$ for different values of Da. It is clearly seen that increasing Da slightly enhances the secondary velocity component. This trend is associated with the reduction in porous resistance at higher permeability levels. As resistance decreases, the fluid encounters less opposition in both axial and transverse directions, thereby strengthening the cross-flow velocity. Nevertheless, the increase remains limited because of the competing influences of magnetic damping and rotational forces. Figure 6c illustrates the temperature distribution corresponding to various values of the Darcy

parameter. It is evident that increasing Da decreases the temperature profile θ(η). This reduction occurs because greater permeability improves fluid transport, which in turn enhances convective heat transfer. The strengthened convection removes thermal energy more effectively from the surface region, resulting in a thinner thermal boundary layer and consequently lower temperature distributions throughout the flow domain.

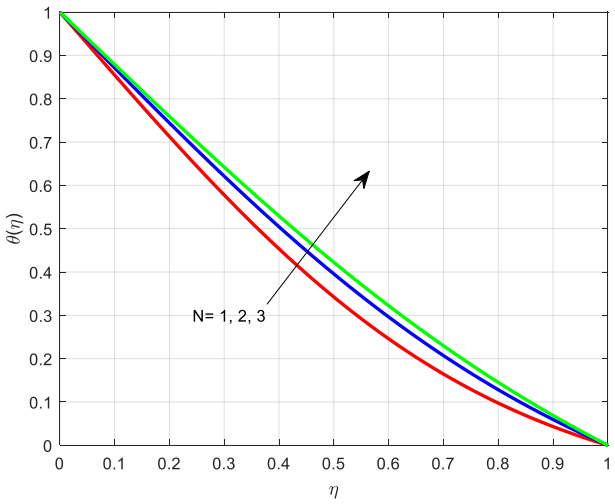

Fig.7 Influence of Radiation Parameter N on Temperature Characteristics.

Figure 7 illustrates the effect of the thermal radiation parameter N on the temperature distribution. It is clearly observed that increasing values of N produce a considerable rise in the temperature profile $\theta(\eta)$. This phenomenon occurs because thermal radiation contributes additional energy transport within the fluid region. An increase in the radiation parameter improves the effective thermal conductivity, enabling a larger amount of heat to remain within the flow field. As a result, the thermal boundary layer becomes thicker, and the temperature increases throughout the entire flow domain.

Table 2: Validation of the present numerical results through comparison with Chamkha et al. [5]

ϕ (%)	Re	Nu (Chamkha et al. [5])	Present Nu	Absolute Error
0	0.1	1.07650	1.07838	0.00188
0	0.5	1.40437	1.40366	0.00071
0	1.0	1.81603	1.81310	0.00293
0	1.5	2.20219	2.20133	0.00086
5	0.1	1.29872	1.29862	0.00010
5	0.5	1.61931	1.61905	0.00026
5	1.0	2.02732	2.02652	0.00080
5	1.5	2.42441	2.42254	0.00187
10	0.1	1.57195	1.57385	0.00190
10	0.5	1.88889	1.88947	0.00058
10	1.0	2.29326	2.29286	0.00040
10	1.5	2.69399	2.69197	0.00202

To validate the accuracy of the present numerical method, the computed Nusselt number is compared with the results reported by Chamkha et al. [5] under limiting conditions (Mn = 0, Ec = 0, and absence of porous effects). The results show excellent agreement with negligible error, confirming the reliability and accuracy of the present bvp4c-based numerical solution. It is also noted that when the Darcy parameter is neglected (Da → ∞), the present model reduces to the classical model of Chamkha et al. [5].

Table 3: Computation of skin friction and Nusselt number for distinct flow parameter.

A	Re	Mn	Ro	Da	N	Skin Friction Coefficient (C_f)	Nusselt Number (Nu)
-2						12.478046	-0.955863
-1						8.670179	-0.639304
0						3.844582	-0.253185
1						-2.004396	0.102835
2						-8.853895	0.379765
	1					-2.004396	0.102835
	4					-2.684175	1.245570
	7					-3.285049	2.019285
		0				-2.043312	0.121205
		5				-1.871284	0.032106
		10				-1.743324	-0.051712
			1			-2.025287	0.102326
			3			-2.249729	0.097020
			5			-2.705790	0.086995
				1		-1.934954	0.101352
				2		-1.978322	0.102279
				5		-2.004396	0.102835
					1	---------	1.062538
					2	---------	2.750182
					3	---------	4.335341

VI. CONCLUSION

In the current investigation, the magnetohydrodynamic flow and thermal transport behavior of an $Ag - GO/H_2O - EG$ (50: 50) hybrid nanofluid in a rotating porous configuration between parallel plates has been analyzed. The governing nonlinear equations were converted into dimensionless form and solved numerically through the MATLAB-based bvp4c technique. The impacts of important physical parameters, including suction/injection parameter, Reynolds number, magnetic parameter, rotation parameter, Darcy parameter, and thermal radiation parameter, were examined comprehensively. The findings indicate that suction enhances both axial and secondary velocity distributions while considerably decreasing temperature profiles, whereas injection exhibits the reverse trend because of increased boundary layer growth. A rise in the Reynolds number intensifies axial flow but weakens secondary motion and reduces thermal boundary layer thickness. The magnetic parameter generates a resistive Lorentz force that suppresses the velocity components while increasing temperature due to intensified Joule heating effects. The rotation parameter redistributes momentum within the flow field, resulting in reduced axial velocity and enhanced secondary velocity, together with a slight increase in temperature distribution. Moreover, the introduction of porous medium effects through the Darcy parameter demonstrates that greater permeability (higher Da) lowers flow resistance, thereby improving velocity profiles while simultaneously increasing temperature because of enhanced convective heat transfer. The thermal radiation parameter notably elevates the temperature field by strengthening the effective thermal energy within the fluid region. Overall, the combined influence of magnetic effects, rotational motion, and porous medium characteristics plays an important role in regulating flow dynamics and heat transfer behavior. The present analysis confirms that the incorporation of Ag–GO hybrid nanoparticles together with porous medium influences can significantly improve thermal performance, making the model valuable for advanced thermal engineering and energy-related applications. The results further reveal that heat transfer characteristics are strongly dependent on magnetic effects, rotational behavior, and porous medium properties. In particular, stronger porous resistance (lower Darcy number) decreases the Nusselt number because of intensified drag effects.

REFERENCES

[1] S.U. Choi, J.A. Eastman, Enhancing Thermal Conductivity of Fluids with Nanoparticles (No. ANL/MSD/CP-84938; CONF-951135-29), Argonne National Lab., IL (United States), 1995.

[2] S. Suresh, K. Venkitaraj, P. Selvakumar, M. Chandrasekar, Experimental investigation of mixed convection with synthesis of Al2O3 using two step method and its thermo physical properties, Colloid. Surface. 8 (2011) 41–48.

[3] M. Mustafa, T. Hayat, and S. Obaidat, "On heat and mass transfer in the unsteady squeezing flow between parallel plates," Meccanica 47, 1581–1589 (2012).

[4] S. Dogonchi, M. Alizadeh, and D. D. Ganji, "Investigation of MHD Go-water nanofluid flow and heat transfer in a porous channel in the presence of thermal radiation effect," Adv. Powder Technol. 28, 1815–1825 (2017).

[5] Chamkha, Ali J., A. S. Dogonchi, and D. D. Ganji. "Magneto-hydrodynamic flow and heat transfer of a hybrid nanofluid in a rotating system among two surfaces in the presence of thermal radiation and Joule heating." Aip Advances 9, no. 2 (2019).

[6] R. Mashayekhi, E. Khodabandeh,O.A.Akbari,D.Toghraie, M.Bahiraei, and M. Gholami, "CFD analysis of thermal and hydrodynamic characteristics of hybrid nanofluid in an ewdesignedsinusoidal double-layered microchannel heat sink," J. Therm. Anal. Calorim. 134, 2305–2315 (2018).

[7] R. S. R. Gorla, S. Siddiqa, M. A. Mansour, A. M. Rashad, and T. Salah, "Heat source/sink effects on a hybrid nanofluid-filled porous cavity," J. Thermophys Heat Transfer (2017).

[8] S. Dogonchi, D. D. Ganji, and O. D. Makinde, "Impact of stretching and penetration of walls on nanofluid flow and heat transfer in a rotating system," Defect Diffus. Forum 387, 37–50 (2018).

[9] Y. Lin and L. Zheng, "Effects of Brownian motion and thermophoresis on nanofluids in a rotating circular groove: A numerical simulation," Int. J. Heat Mass Transf. 123, 569–582 (2018).

[10] M. Sheikholeslami, H. R. Ashorynejad, G. Domairry, and I. Hashim, "Flow and heat transfer of Cu-water nanofluid between a stretching sheet and a porous surface in a rotating system," J. Appl. Math. (2012).

[11] Vajravelu, K. & Kumar, B. V. R. Analytical and numerical solutions of a coupled non-linear system arising in a three-dimensional rotating flow. Int. J. Non-Linear Mech. 39, 13–24 (2004).

[12] Greenspan, H. P. The theory of rotating fluids. CUP Arch. (1968).

[13] Preetham, M. P., and S. Kumbinarasaiah. "Analysis of hybrid nanofluid MHD flow and heat transfer between two surfaces in a rotating system in the presence of Joule heating and thermal radiation by Fibonacci wavelet." Journal of Nanofluids 13, no. 1 (2024): 1-14.

[14] Shah, Zahir, Muhammad Sulaiman, Abdullah Dawar, Mansoor H. Alshehri, and Narcisa Vrinceanu. "Darcy–Forchheimer MHD rotationally symmetric micropolar hybrid-nanofluid flow with melting heat transfer over a radially stretchable porous rotating disk." Journal of Thermal Analysis and Calorimetry (2024): 1-17.

[15] J. Sarkar, P. Ghosh, A. Adil, A review on hybrid nanofluids: recent research, development, and applications, Renew. Sustain. Energy Rev. 43 (2015) 164–177.

[16] M. Arshad, A. Hassan, Q. Haider, F. M. Alharbi, N. Alsubaie, A. Alhushaybari, D.-P. Burduhos-Nergis, and A. M. Galal, Nanomaterials 12, 4177 (2022), DOI: 10.3390/nano12234177.

[17] G. M. Moatimid, M. A. A. Mohamed, and K. Elagamy, Sci. Rep. 12, 11275 (2022), DOI: 10.1038/s41598-022-15094-w.

[18] M.W. Tian, S. Rostami, S. Aghakhani, A.S. Goldanlou, C. Qi, A techno-economic investigation of 2D and 3D configurations of fins and their effects on heat sink efficiency of MHD hybrid nanofluid with slip and non-slip flow, Int. J. Mech. Sci. 189 (2021), 105975.

[19] N.C. Roy, M. Hossain, I. Pop, Analysis of dual solutions of unsteady micropolar Hybrid nanofluid flow over a stretching/shrinking sheet, J. Appl. Comput. Mechan. 7 (1) (2021) 19–33.

[20] Fazeli, M.R.S. Emami, A. Rashidi, Investigation, and optimization of the behavior of heat transfer and flow of MWCNT-CuO hybrid nanofluid in a brazed plate heat exchanger using response surface methodology, Int. Commun. Heat Mass Tran. 122 (2021), 105175

[21] R. Alizadeh, J.M.N. Abad, A. Fattahi, M.R. Mohebbi, M.H. Doranehgard, L.K. Li, N. Karimi, A machine learning approach to predicting the heat convention and thermodynamics of an external flow of hybrid nanofluid, J. Energy Resour. Technol. 143 (7) (2021).

[22] K.G. Kumar, E.H.B. Hani, M.E.H. Assad, M. Rahimi-Gorji, S. Nadeem, A novel approach for investigation of heat transfer enhancement with ferromagnetic hybrid nanofluid by considering solar radiation, Microcyst. Technol. 27 (1) (2021) 97–104.

[23] Aziz, W. Jamshed, T. Aziz, H.M. Bahaidarah, K.U. Rehman, Entropy analysis of Powell–Eyring hybrid nanofluid including effect of linear thermal radiation and viscous dissipation, J. Therm. Anal. Calorim. 143 (2) (2021) 1331–1343.

[24] Yasmin, K. Ali, M. Ashraf, MHD Casson nanofluid flow in a square enclosure with non-uniform heating using the Brinkman model, Eur. Phys. J. Plus 136 (2) (2021) 1–14.

[25] S. Siddiqa, N. Begum, M.A. Hossain, M.N. Abrar, R.S.R. Gorla, Q. Al-Mdallal, Effect of thermal radiation on conjugate natural convection flow of a micropolar fluid along a vertical surface, Comput. Math. Appl. 83 (2021) 74–83.

[26] N. A. Yacob, N. F. Dzulkifli, S. N. A. Salleh, A. Ishak, and I. Pop, Mathematics 10, 7 (2022), DOI: 10.3390/ math10010007.

[27] M. Shoaib, F. Ali, I. Khan, *et al.*, "Three-dimensional MHD radiative flow of hybrid nanofluid over an extending surface," *Scientific Reports*, vol. 10, Art. no. 17080, 2020.

[28] I. Waini, A. Ishak, and I. Pop, "MHD hybrid nanofluid flow over a permeable stretching/shrinking surface with radiation effect," *Applied Mathematics and Mechanics*, vol. 41, pp. 507–520, 2020.

[29] M. Shoaib, M. A. Z. Raja, I. Khan, *et al.*, "Hybrid nanofluid flow over a rotating disk with Joule heating and thermal radiation," *Alexandria Engineering Journal*, vol. 60, no. 5, pp. 4325–4338, 2021.

[30] S. Abu Bakar, N. Bachok, N. M. Arifin, *et al.*, "Hybrid nanofluid flow in a porous medium with radiation and heat generation," *Case Studies in Thermal Engineering*, vol. 25, Art. no. 100918, 2021.

[31] A. M. Rashad, "MHD hybrid nanofluid flow in porous media with thermal radiation and heat source," *Arabian Journal for Science and Engineering*, vol. 48, pp. 12345–12358, 2023.